CERES_EBAF-Surface_Ed2.6r

Data Quality Summary (November 1, 2012)

Investigation: **CERES**
Data Product: **EBAF-Surface**

Data Set: **Terra (Instruments: CERES-FM1 or CERES-FM2)**
Aqua (Instruments: CERES-FM3 or CERES-FM4)

Data Set Version: **Edition2.6r**

Subsetting Tool Availability: http://ceres.larc.nasa.gov

The purpose of this document is to inform users of the accuracy of this data product as determined by the CERES Science Team. The document summarizes key validation results, provides cautions where users might easily misinterpret the data, provides links to further information about the data product, algorithms, and accuracy, and gives information about planned data improvements. This document also automates registration in order to keep users informed of new validation results, cautions, or improved data sets as they become available.

This document provides a high-level quality assessment of the CERES EBAF-Surface data product that contains surface fluxes consistent with the top-of-atmosphere fluxes contained in the CERES Energy Balanced and Filled (EBAF-TOA) data product. As such, this document represents the minimum information needed by scientists for appropriate and successful use of the CERES EBAF-Surface data product. For a more thorough description of the methodology used to produce EBAF-Surface, please see Kato et al. (2012a). It is strongly suggested that authors, researchers, and reviewers of research papers re-check this document for the latest status before publication of any scientific papers using this data product.

NOTE: To navigate the document, use the Adobe Reader bookmarks view option. Select "View" "Navigation Panels" "Bookmarks".

TABLE OF CONTENTS

Section Page

LIST OF FIGURES

Figure Page

LIST OF FIGURES

Figure Page

LIST OF TABLES

Table Page

1.0 Introduction

In order to determine the distribution of surface radiation over the globe, the CERES team relies on radiative transfer model calculations initialized using satellite-based cloud and aerosol retrievals and meteorological and aerosol assimilation data from reanalysis to characterize the atmospheric state. The accuracy and stability in computed top-of-atmosphere (TOA) and surface fluxes thus depend upon the quality of the input cloud and atmospheric data (e.g. Rose et al. 2012). The standard CERES data products (e.g., SYN1deg_Month) use cloud and aerosol properties derived from MODIS radiances, meteorological assimilation data from the Goddard Earth Observing System (GEOS) Versions 4 and 5 models, and aerosol assimilation from the Model for Atmospheric Transport and Chemistry (MATCH; Collins et al. 2001).

In order to minimize the error in surface fluxes due to uncertainties in the input data sources, the EBAF-Surface data product introduces several additional constraints based upon information from other independent data sources, such as CERES TOA fluxes, AIRS-derived temperature/humidity profiles, and CALIPSO/Cloudsat-derived vertical profiles of clouds.

This document describes the procedure used to determine EBAF surface fluxes and provides an assessment of the uncertainty of the EBAF-Surface product.

2.0 Description of Data Used for EBAF-Surface Production

Surface fluxes in EBAF-Surface are derived from two CERES data products: (i) CERES SYN1deg-Month_Ed2 provides computed surface fluxes to be adjusted and (ii) CERES EBAF-TOA_Ed2.6r (Loeb et al. 2009, Loeb et al. 2012) provides the CERES-derived TOA flux constraints by observations.

SYN1deg-Month is a Level 3 product and contains gridded monthly mean computed TOA and surface fluxes along with fluxes at three atmospheric pressure levels (70, 200, and 500 hPa). Surface fluxes in SYN1deg-Month are computed with cloud properties derived from MODIS and geostationary satellites (GEO). Each geostationary satellite instrument is calibrated against MODIS (Doelling et al. 2012). The Ed2 CERES cloud algorithm (Minnis et al. 2011) derives cloud properties (e.g. fraction, optical depth, top height, and particle size) from narrowband radiances measured by MODIS twice daily from March 2000 through August 2002 (Terra only) and four times a day after September 2002 (Terra plus Aqua). The Edition 2 two-channel GEO cloud algorithm (Minnis et al. 1995) provides cloud properties (fraction, top height, and daytime optical depth) every three hours between Terra and Aqua observations. Cloud properties are gridded onto a 1°×1° spatial grid and interpolated to 1 hourly intervals (hour boxes) to fill hour boxes with no retrieved cloud properties. Up to four cloud-top heights (cloud types) are retained for each hour box within a 1°×1° grid box. Cloud properties (cloud top height, optical thickness, particle size, phase etc.) are kept separately for four cloud types.

To treat horizontal variability of optical thickness within a cloud type explicitly, both linear and logarithmic means of cloud optical thicknesses are computed for each cloud type. The distribution of cloud optical thickness expressed as a gamma distribution is estimated from the linear and logarithmic cloud optical thickness means (Barker 1996; Oreopoulos and Barker 1999; Kato et al. 2005). Once the distribution of cloud optical thickness is estimated for each cloud type, a gamma-weighted two-stream radiative transfer model (Kato et al. 2005) is used to compute the shortwave flux vertical profile for each cloud type. The logarithmic mean optical thickness is used in the longwave flux computation with a modified 2-stream approximation (Toon et al. 1989; Fu et al. 1997). The cloud base height, which largely influences the surface downward longwave flux in midlatitude and polar regions, is estimated by an empirical formula described by Minnis et al. (2011).

Temperature and humidity profiles used in the radiative transfer model calculations are from the Goddard Earth Observing System (GEOS-4 and 5) Data Assimilation System reanalysis (Bloom et al. 2005; Rienecker et al. 2008). GEOS-4 is used from March 2000 through October 2007, and GEOS-5 is used beginning November 2007. The GEOS-4 and 5 temperature and relative humidity profiles have a temporal resolution of 6 hours. Spatially, the profiles are re-gridded to 1°×1° maps. Skin temperatures used in the computations are from GEOS-4 and GEOS-5 at a 3-hourly resolution, the native temporal resolution of GEOS-4 skin temperature, although the GEOS-5 product has a higher 1-hourly native resolution available. Other inputs used in SYN1deg-Month include ozone amount (Yang et al. 2000) and ocean spectral surface albedo from Jin et al. (2004). Broadband land surface albedos are inferred from the clear-sky TOA albedo derived from CERES measurements (Rutan et al. 2009).

Computed TOA fluxes from SYN1deg-Month do not necessarily agree with the CERES-derived TOA fluxes from EBAF-TOA_Ed2.6r, partly because of the error in inputs used in the computations. Input errors also affect computed surface fluxes. To minimize the error in surface fluxes, we adjust surface, atmospheric, and cloud properties using CERES-derived TOA fluxes as constraint. To constrain computed TOA fluxes by CERES-derived TOA fluxes, we first determine the difference of the computed TOA fluxes from SYN1deg-Month and the CERES-derived TOA fluxes from EBAF-TOA, using the monthly means on the 1°×1° grid. Second, we correct the TOA longwave bias error caused by the upper tropospheric relative humidity error using AIRS (AIRX3STM.005) data. We also correct for the bias error of the surface downward longwave flux, which is caused by missing lower clouds of overlapping clouds. This bias correction is based on computed surface fluxes that used inputs of CALIPSO- and CloudSat-derived vertical cloud profiles (Kato et al. 2011). Third, we use a Lagrange multiplier procedure to determine the perturbation of surface, cloud, and atmospheric properties to match the TOA flux differences, assuming that changes applied to the input variables are small relative to their respective monthly mean values. Jacobians that are needed to determine surface, cloud, and atmospheric property perturbations, as well as surface flux adjustments, are computed separately and used in the Lagrange multiplier procedure. Fourth, we compute the surface flux change based on perturbed surface, cloud, and atmospheric properties. Subsequently, the surface flux changes are added to 1°×1° monthly mean SYN1deg-Month fluxes.

3.0 Cautions and Helpful Hints

The CERES Science Team notes several CAUTIONS and HELPFUL HINTS regarding the use of CERES_EBAF-Surface_Ed2.6r:

- The CERES_EBAF-Surface_Ed2.6r product can be visualized, subsetted, and ordered from: (http://ceres.larc.nasa.gov).
- The CERES team has significantly reduced GEO artifacts in CERES_EBAF-Surface_Ed2.6r as compared to surface fluxes included in SYN1deg-Month.
- CERES_EBAF-Surface_Ed2.6r does not contain TOA fluxes. Corresponding TOA fluxes are included in CERES_EBAF-TOA_Ed2.6r.
- Clear-sky surface fluxes are consistent with clear-sky TOA fluxes included in CERES-EBAF-TOA_Ed2.6r. Therefore clear-sky fluxes are clear-sky fraction-weighted fluxes instead of fluxes computed by removing clouds. Computed clear-sky fluxes are also constrained by CERES-derived clear-sky fluxes that are included in CERES_EBAF-TOA_Ed2.6r.
- Global means are determined using zonal geodetic weights. The zonal geodetic weights can be obtained from (http://ceres.larc.nasa.gov/science_information.php?page=GeodeticWeights).
- Cloud radiative effects are computed by all-sky flux minus clear-sky flux.
- The net flux is positive when the energy is deposited to the surface, i.e. the net is defined as downward minus upward fluxes.
- The source of temperature and humidity profiles for surface flux calculations changes from GEOS-4 to GEOS-5 starting in November 2007. When deseasonalized anomalies are calculated separately for land and ocean, the time series of deseasonalized surface fluxes shows a discontinuity between October 2007 and November 2007.
- When clear-sky upward longwave fluxes are subtracted from all-sky upward longwave fluxes, a large difference appears over Tibet due to the clear-sky sampling discussed in Section 4.3 this document.
- Clear-sky net shortwave flux is sometimes negative in polar regions (north of 60°N and south of 60°S). In other words, the upward shortwave flux is greater than downward shortwave flux. This is frequently caused by the constraint to the TOA flux near the terminator where twilight flux (Kato and Loeb 2003) has been added to reflected shortwave flux for EBAF-TOA. Note that the negative clear-sky net shortwave flux also affects the cloud effect to the net shortwave surface flux.
- Near surface temperature and humidity inaccuracies exist in GEOS-4 over tropics in 2000 and 2004. For this reason, deseasonalized anomalies of downward longwave irradiance are larger than those found in other comparable global radiation products when 10-year means are used to compute the deseasonalized anomalies.
- An error exists in the regional 1°×1° gridded data. They typically are shifted eastward by 1 degree. The shift is larger near the poles because the shift is by 1 equal-area grid box. Information on the correction is provided here. The correction package consists of an ascii file containing both the incorrect and correct latitudes and longitudes (two 180×360 arrays) and an IDL code to implement the correction.

4.0 Accuracy and Validation

In this section, surface flux uncertainty and known problems of surface fluxes included in the CERES_EBAF-Surface_Ed2.6r product are discussed.

4.1 Global Annual Mean Flux Comparison

Table 4-1 shows that the input adjustments discussed in Section 2 reduce the computed and CERES-derived global annual mean TOA flux difference from -2.3 W m^{-2} to 0.1 W m^{-2} for longwave and from -1.2 W m^{-2} to -0.1 W m^{-2} for shortwave. As a result, the global annual mean surface upward and downward longwave fluxes change by 0.5 W m^{-2} and 1.9 W m^{-2}, respectively. Similarly, the surface upward and downward shortwave fluxes change by 0.8 W m^{-2} and -0.5 W m^{-2}, respectively. These changes are within the uncertainties of the surface fluxes estimated by Kato et al. (2012b), shown in Table 4-3. Note that computed TOA fluxes are not included in the EBAF-Surface product. Users who need TOA fluxes should use the EBAF-TOA product.

Table 4-1. Global annual mean fluxes using data from March 2000 through February 2010 (W m^{-2}).

	Flux Component	Ed 2 SYN1deg-Month	EBAF-Surface Ed2.6r	EBAF-TOA Ed2.6r
TOA	Incoming solar	339.9	339.9	339.9
	LW (all-sky)	237.3	239.7	239.6
	SW (all-sky)	98.5	99.6	99.7
	Net (all-sly)	4.06	0.64	0.57
	LW (clear-sky)	263.7	265.8	265.9
	SW (clear-sky)	52.5	52.5	52.5
	Net (clear-sly)	23.6	21.6	21.5
Surface	LW down (all-sky)	341.8	343.7	
	LW up (all-sky)	397.6	398.1	
	SW down (all-sky)	187.2	186.7	
	SW up (all-sky)	23.3	24.1	
	Net (all-sky)	108.1	108.3	
	LW down (clear-sky)	313.5	314.1	
	LW up (clear-sky)	396.6	398.3	
	SW down (clear-sky)	242.4	243.4	
	SW up (clear-sky)	28.7	29.6	
	Net (clear-sky)	130.6	129.6	

Table 4-2. Estimated uncertainties (1σ or k = 1) in the flux computed with satellite-derived cloud and aerosol properties in W m^{-2} (Kato et al. 2012b).

			Estimated uncertainty			
		Mean value	Monthly gridded	Monthly zonal	Monthly global	Annual global
Downward longwave	Ocean+land	345	14	11	7	7
	Ocean	354	12	10	7	7
	Land	329	17	15	8	7
Upward longwave	Ocean+Land	398	15	8	3	3
	Ocean	402	13	9	5	5
	Land	394	19	15	5	4
Downward shortwave	Ocean+Land	192	10	8	6	4
	Ocean	190	9	8	5	4
	Land	203	12	10	7	5
Upward shortwave	Ocean+Land	23	11	3	3	3
	Ocean	12	11	3	3	3
	Land	53	12	8	6	6

4.2 Regional Mean All-Sky Surface Fluxes

The source of temperature and humidity profiles for flux computations in the SYN1deg-Month product is switched from GEOS-4 to GEOS-5 starting in November 2007. As a result, when deseasonalized anomalies are computed for land and ocean separately, the time series of deseasonalized anomalies show a discontinuity between October 2007 and November 2007 (Figure 4-1). When anomalies are computed for land and ocean together, however, the discontinuity is not apparent (Figure 4-3) because the artifacts over land and ocean cancel one another. Even though the discontinuity is not apparent, users are advised to carefully analyze such time series.

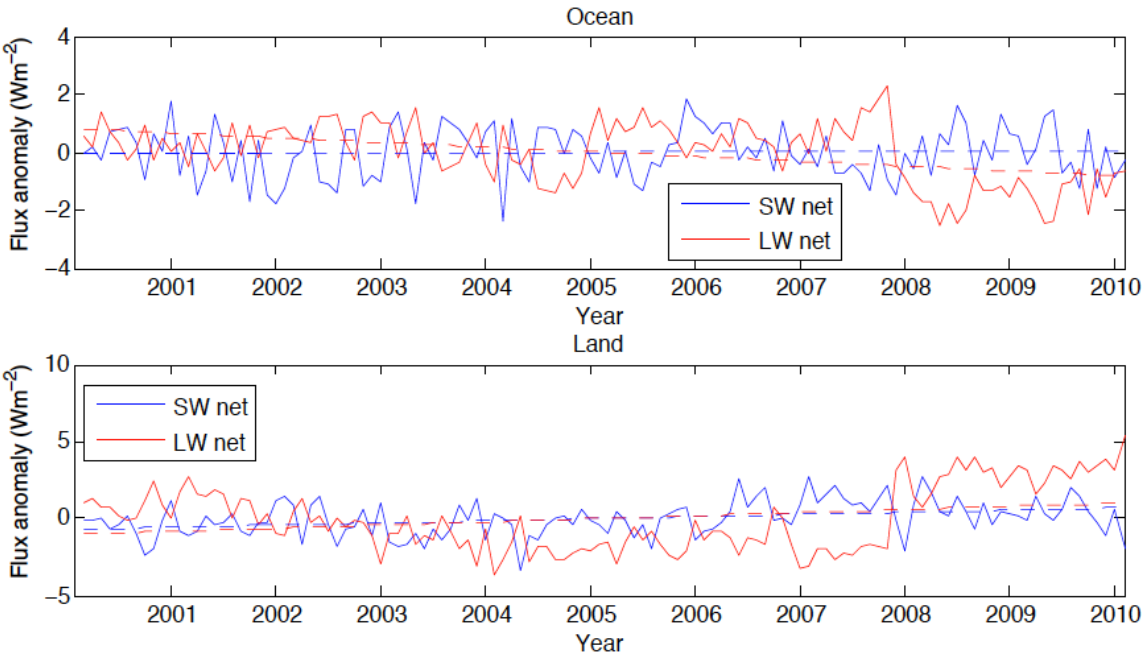

Figure 4-1. Time series of deseasonalized anomalies of global ocean (top) and land (bottom) surface net shortwave (blue) and net longwave (red) fluxes. The discontinuity from October 2007 to November 2007 is apparent. Temperature and relative humidity profiles from GEOS-4 are replaced by GEOS-5 beginning in November 2007.

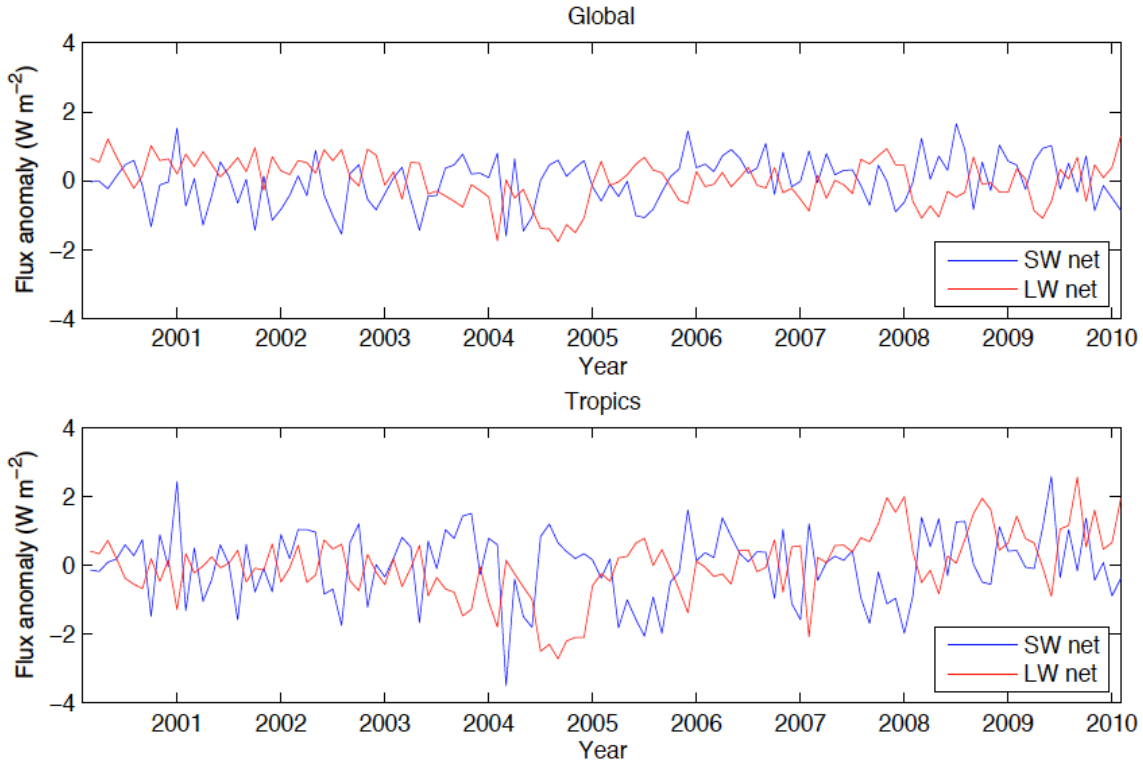

Figure 4-2. Time series of deseasonalized anomalies of global (top) and tropical (bottom) surface net shortwave (blue) and net longwave (red) fluxes.

Cloud properties derived from geostationary satellites (GEO) are used between 60°N to 60°S to resolve diurnal cycles. Although most GEO artifacts are removed, they are apparent when flux differences are computed, such as atmospheric flux (TOA net minus surface net) or cloud radiative effects (all-sky minus clear-sky fluxes). Figure 4-5 (left plot) shows an example of an artifact that appears south of Australia. In addition, when the trend of flux is derived from 1°×1° gridded deseasonalized anomalies, artifacts are often apparent (Figure 4-5 right).

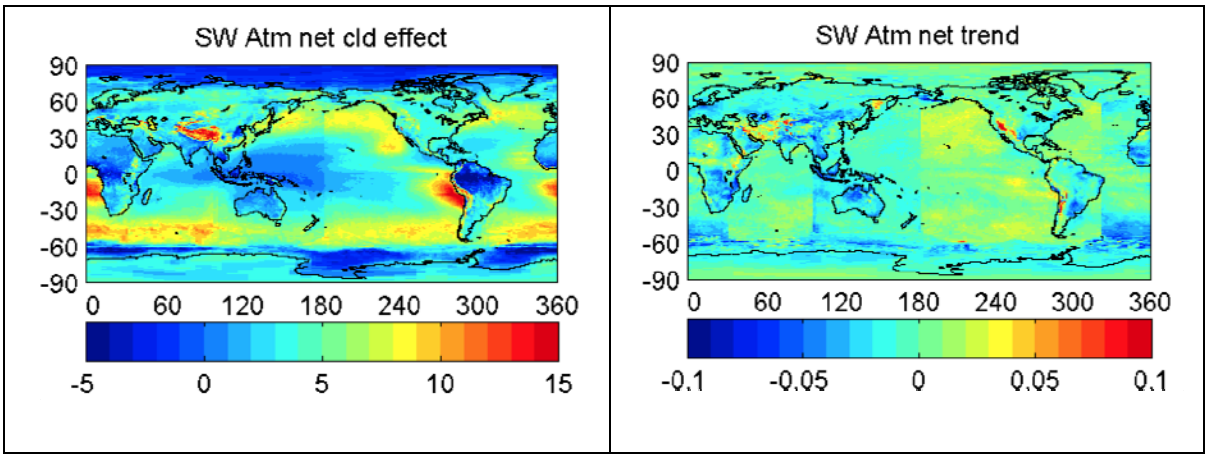

Figure 4-3. (Left) Annual mean within-atmosphere absorbed shortwave cloud radiative effect (W m^{-2}) that are computed by first taking the TOA shortwave net flux minus surface shortwave net flux for both all-sky and clear-sky conditions and by then taking all-sky minus clear-sky values. The cloud effect is computed using 1°×1° gridded 10 years of data. (Right) Trend derived from absorbed shortwave flux by the atmosphere. The trend is expressed in W m^{-2} per month.

4.3 Regional Mean Clear-Sky Surface Fluxes

To be consistent with CERES_EBAF-TOA, the 1°×1° gridded monthly computed mean surface clear-sky fluxes are averaged by weighting by the clear-sky fraction. As a result, the monthly gridded mean clear-sky surface flux can be significantly different from the clear-sky flux computed by removing clouds. Figure 4-7, Figure 4-9, and Figure 4-11 show the difference of clear-sky surface fluxes computed using clear-sky fraction weights and those computed by removing clouds. The difference of longwave fluxes is caused by a smaller water vapor amount in clear-sky atmospheres than the amount in all-sky conditions (e.g. Cess and Potter 1987; Sohn et al. 2010). Relatively larger differences of shortwave fluxes predominantly occur over polar regions and are caused by the different sampling of the cryosphere surface; if clear-sky predominantly occurs over open ocean versus sea ice, surface shortwave fluxes would be different from those computed by removing clouds.

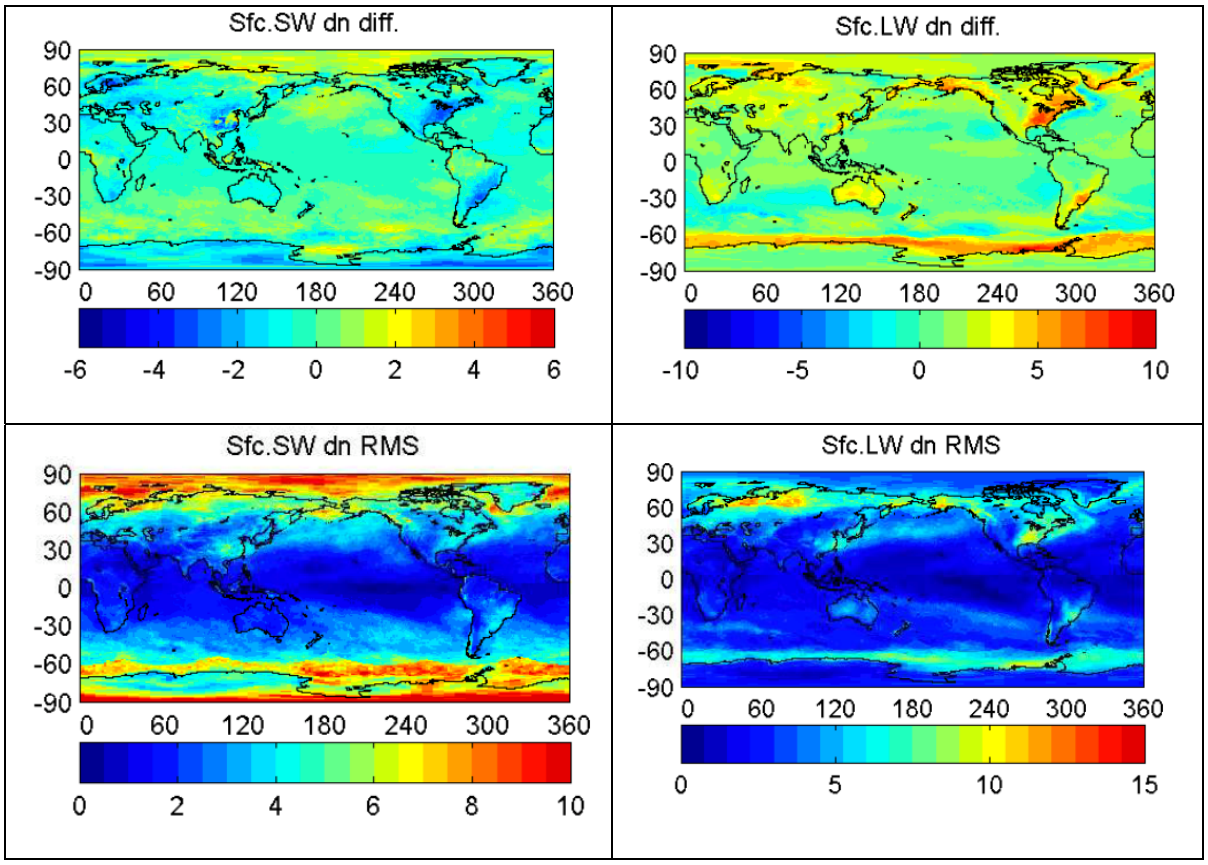

Figure 4-4. (Top) Difference, defined as clear-sky fluxes computed with clouds removed minus clear-sky fraction-weighted fluxes, of clear-sky surface downward shortwave (left) and downward longwave (right) fluxes in W m^{-2}. Differences are computed using 10 years of monthly 1°×1° gridded mean fluxes from March 2000 through February 2010. (Bottom) RMS difference of cloud-removed and clear-sky fraction-weighted surface downward shortwave fluxes (left) and surface downward longwave fluxes (right) in W m^{-2}, also computed using 10 years of monthly 1°×1° gridded mean fluxes.

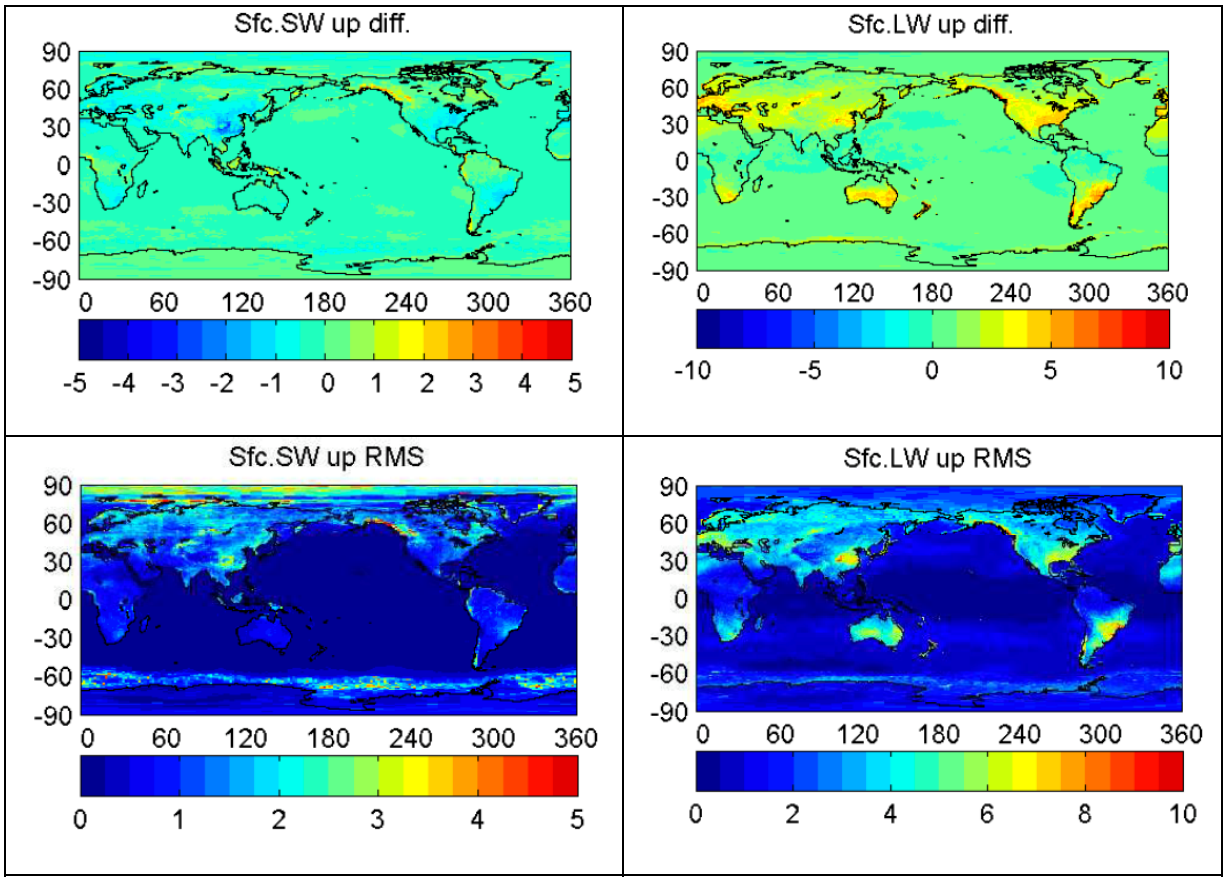

Figure 4-5. (Top) Difference, defined as clear-sky fluxes computed with clouds removed minus clear-sky fraction-weighted fluxes, of clear-sky surface upward shortwave (left) and upward longwave (right) fluxes in W m^{-2}. Differences are computed using 10 years of monthly 1°×1° gridded mean fluxes from March 2000 through February 2010. (Bottom) RMS difference of cloud-removed and clear-sky fraction-weighted surface upward shortwave fluxes (left) and surface upward longwave fluxes (right) in W m^{-2}, also computed using 10 years of monthly 1°×1° gridded mean fluxes.

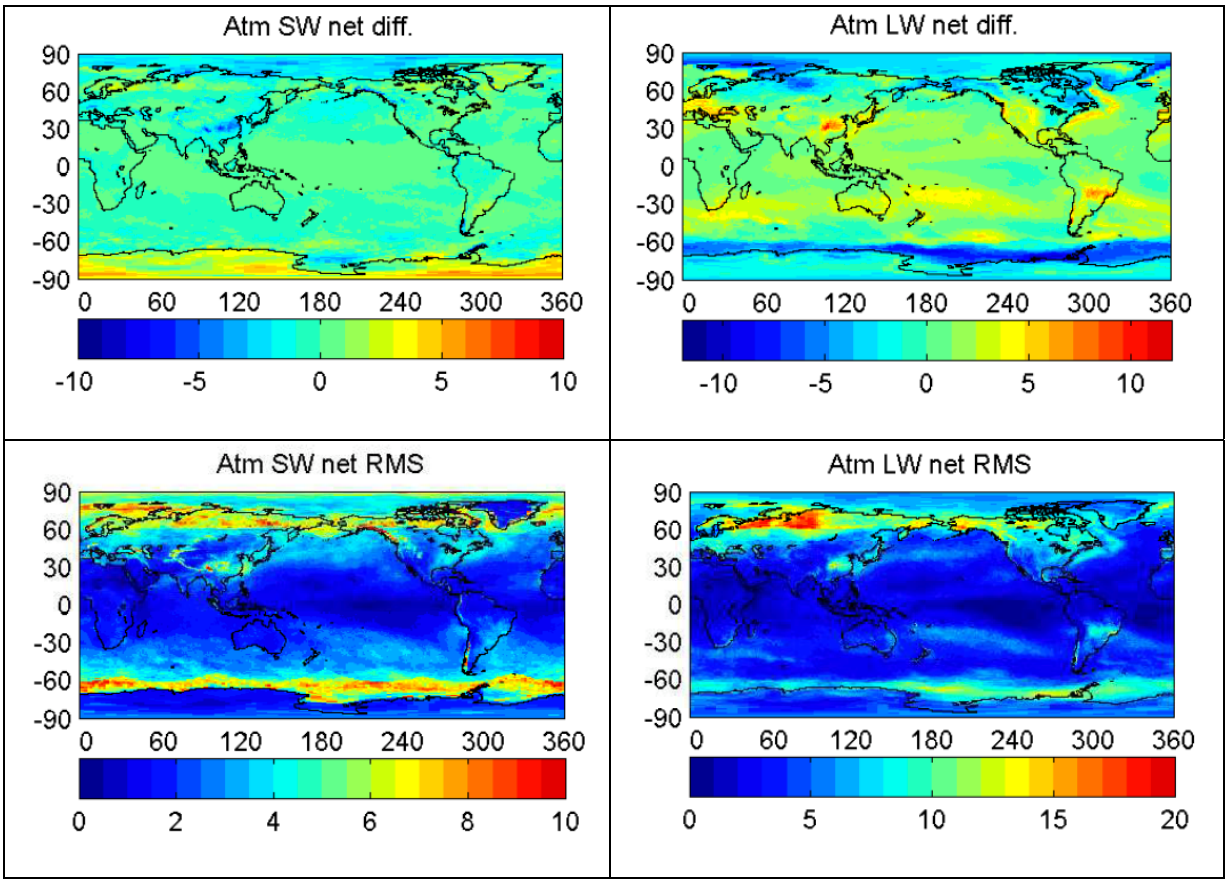

Figure 4-6. (Top) Difference, defined as clear-sky fluxes computed with clouds removed minus clear-sky fraction-weighted fluxes, of clear-sky atmospheric net (TOA net minus surface net) shortwave (left) and clear-sky atmospheric net longwave (right) fluxes in W m^{-2}. Differences are computed using 10 years of monthly 1°×1° gridded mean fluxes from March 2000 through February 2010. (Bottom) RMS difference of cloud-removed and clear-sky fraction-weighted atmospheric net shortwave fluxes (left) and atmospheric net longwave fluxes (right) in W m^{-2}, also computed using 10 years of monthly 1°×1° gridded mean fluxes.

Constraining clear-sky fraction-weighted computed flux instead of cloud-removed clear-sky fluxes helps to achieve a better agreement with CERES-derived clear-sky TOA fluxes. However, some regions over land (e.g. Tibet shown in Figure 4-13 bottom) show a large difference in surface upward longwave fluxes between clear-sky and all-sky conditions. As a result, when the clear-sky flux is subtracted from the all-sky flux, the apparent cloud effect on surface upward longwave fluxes is large. This is caused by an independent constrainment of TOA clear-sky and all-sky fluxes, which also show a large difference over Tibet (Figure 4-13 top). The reason for the large clear-sky and all-sky TOA upward longwave flux difference is sampling. The day-night temperature difference over Tibet is relatively large. Because of more cloud cover during nighttime Terra overpasses, most clear-sky samplings come from warmer daytime (Figure 4-15). This gives a large clear-sky TOA upward longwave flux over Tibet. A large flux difference of

surface upward longwave flux under clear-sky and all-sky conditions at the coast of Antarctica is caused by a relatively large adjustment of surface temperatures to match CERES TOA clear-sky fluxes.

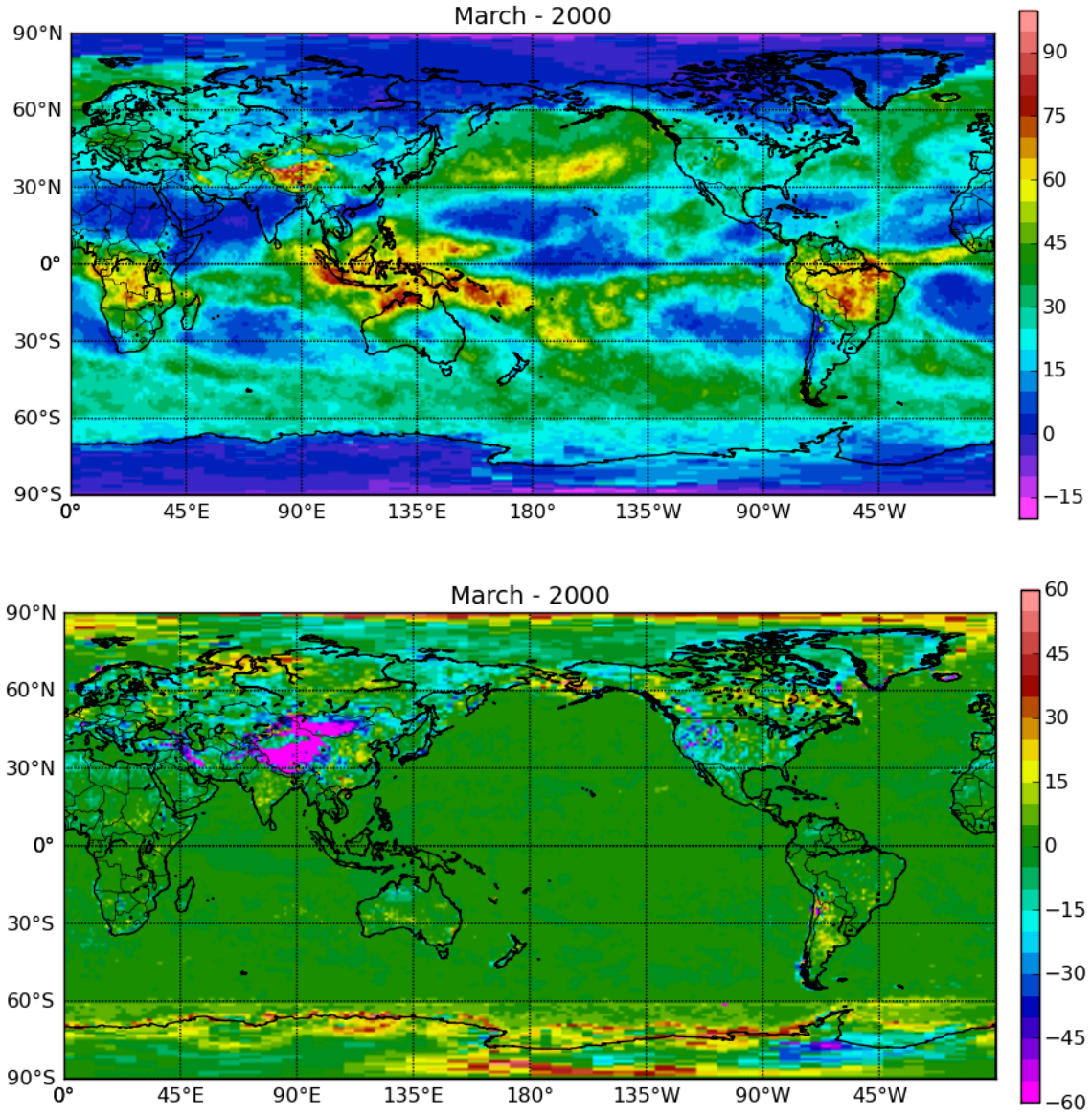

Figure 4-7. (Top) TOA cloud longwave radiative effect computed by subtracting clear-sky TOA upward longwave flux from all-sky TOA upward longwave flux for March 2000. (Bottom) The difference of the surface upward longwave flux under all-sky and clear-sky conditions (all-sky minus clear-sky) for March 2000. Large negative values over Tibet are caused by matching TOA CERES-derived longwave flux to the EBAF-TOA value independently for all-sky and clear-sky conditions. Clear-sky samplings occur predominantly during daytime when surface temperatures are high, resulting in a large surface upward longwave flux difference between clear-sky and all-sky conditions.

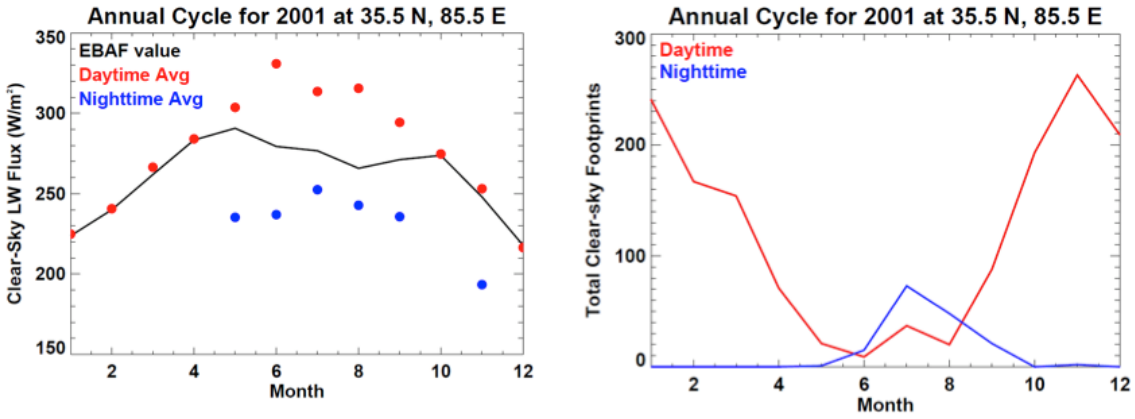

Figure 4-8. (Left) Monthly mean clear-sky CERES-derived TOA flux over Tibet as a function of month from EBAF-TOA (black line). Daytime and nighttime averages are shown by red and blue circles. (Right) Daytime and nighttime clear-sky fraction derived from MODIS over Tibet. Nighttime clear-sky scenes occur infrequently during spring, fall, and winter, causing daytime clear-sky sampling to dominate.

4.4 Comparison with Surface Observations

Figure 4-17. (Left) Comparison of computed surface downward shortwave flux with observed fluxes at 26 surface sites. Each dot represents a monthly mean value. Twenty-six sites located on relatively uniform terrain are selected. Ten years of data from March 2000 through February 2010 are used.

9 summarizes the bias and RMS difference of fluxes from CERES_EBAF-Surface_Ed2.6r compared with surface observations at 26 surface sites. The RMS differences of monthly mean surface downward shortwave and longwave fluxes are less than the uncertainty of monthly gridded fluxes shown in Table 4-3.

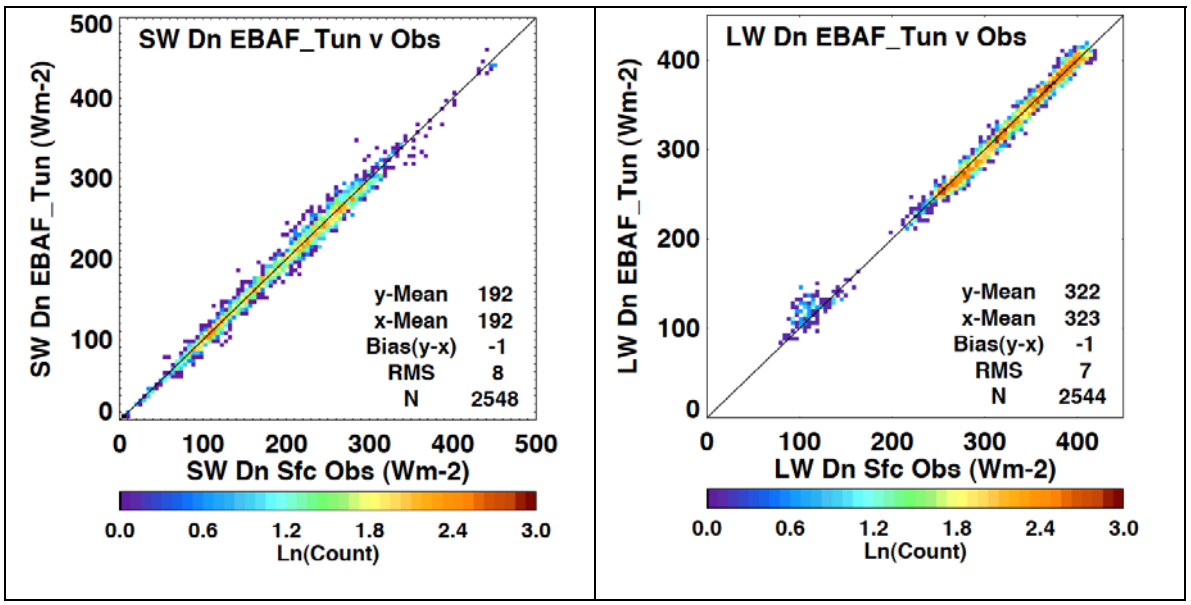

Figure 4-9. (Left) Comparison of computed surface downward shortwave flux with observed fluxes at 26 surface sites. Each dot represents a monthly mean value. Twenty-six sites located on relatively uniform terrain are selected. Ten years of data from March 2000 through February 2010 are used.

5.0 References

The full version of CERES EBAF-Surface_Ed2.6r is available from the following ordering site: http://ceres.larc.nasa.gov/order_data.php

Barker, H. W., 1996: A parameterization for computing grid-averaged solar fluxes for inhomogeneous marine boundary layer clouds. Part I: Methodology and homogeneous biases. *J. Atmos. Sci*, 53, 2289-2303.

Bloom, S. A., and Coauthors, 2005: Documentation and validation of the Goddard Earth Observing System (GEOS) Data Assimilation System Version-4. NASA Tech. Rep. NASA/TM-2005-104606, Vol. 26, 187 pp.

Cess, R. D. and G. L. Potter, 1987: Exploratory studies of cloud radiative forcing with a general circulation model. *Tellus*, 39A, 460-473.

Collins, W. D., P. J. Rasch, B. E. Eaton, B. V. Khattatov, J.-F. Lamarque, and C. S. Zender, 2001: Simulating aerosols using a chemical transport model with assimilation of satellite aerosol retrievals: Methodology for INDOEX. *J. Geophys. Res.*, 106**,** 7313–7336.

Doelling, D. R., N. G. Loeb, D. F. Keyes, M. L. Nordeen, D. Morstad, B. A. Wielicki, D. F. Young, and M. Sun, 2012: Geostationary enhanced temporal interpolation for CERES flux products, submitted to *J. Atmos. Oceanic Technol*.

Fu, Q., K. Liou, M. Cribb, T. Charlock, and A Grossman, 1997: On multiple scattering in thermal infrared radiative transfer. *J. Atmos. Sci*., 54, 2799-2812.

Jin, Z., T. P. Charlock, W. L. Smith, Jr., and K. Rutledge, 2004: A look-up table for ocean surface albedo. *Geophys. Res. Lett.*, 31, L22301.

Kato, S. and N. G. Loeb, 2003: Twilight irradiance reflected by the Earth estimated from Clouds and the Earth's Radiant Energy System (CERES) measurements. *J. Climate*, 16, 2646-2650.

Kato, S., F. G. Rose, and T. P. Charlock, 2005: Computation of domain-averaged irradiance using satellite derived cloud properties. *J. Atmos. Oceanic Technol.*, 22, 146-164.

Kato, S., and Coauthors, 2011: Improvements of top-of-atmosphere and surface irradiance computations with CALIPSO-, CloudSat-, and MODIS-derived cloud and aerosol properties. *J. Geophys. Res*., 116, D19209, doi:10.1029/2011JD016050.

Kato, S., N. G. Loeb, F. G. Rose, D. R. Doelling, D. A. Rutan, T. E. Caldwell, L. Yu, and R. A. Weller, 2012a: Surface irradiances consistent with CERES-derived top-of-atmosphere shortwave and longwave irradiances, *J. Climate*, in press.

Kato, S., N. G. Loeb, D. A. Rutan, F. G. Rose, S. Sun-Mack, W. F. Miller, and Y. Chen, 2012b: Uncertainty estimate of surface irradiances computed with MODIS-, CALIPSO-, and CloudSat-derived cloud and aerosol properties. *Surv. Geophys*., doi:10.1007/s10712-012-9179-x.

Loeb, N. G., B. A. Wielicki, D. R. Doelling, G. L. Smith, D. F. Keyes, S. Kato, N. Manalo-Smith, and T. Wong, 2009: Toward optimal closure of the Earth's top-of-atmosphere radiation budget. *J. Climate*, 22, 748-766.

Loeb, N. G., J. M. Lyman, G. C. Johnson, R. P. Allan, D. R. Doelling, T. Wong, B. J. Soden, and G. L. Stephens, 2012: Observed changes in top-of-the-atmosphere radiation and upper-ocean heating consistent within uncertainty. *Nat. Geosci.*, 5, 110-113. doi:10.1038/NGEO1375.

Minnis, P., W. L. Smith, Jr., D. P. Garber, J. K. Ayers, and D. R. Doelling, 1995: Cloud properties derived from GOES-7 for Spring 1994 ARM intensive observing period using Version 1.0.0 of ARM Satellite Data Analysis Program. NASA Ref. Pub. NASA-RP-1366, 62 pp.

Minnis, P. and Coauthors, 2011: CERES Edition-2 cloud property retrievals using TRMM VIRS and Terra and Aqua MODIS data, Part I: Algorithms. *IEEE Trans. Geosci. Remote Sens.* 49, doi: 10.1109/TGRS.2011.2144601.

Oreopoulos, L. and H. W. Barker, 1999: Accounting for subgrid-scale cloud variability in a multi-layer 1D solar radiative transfer algorithm. *Quart. J. Roy. Meteor. Soc*. 125, 301-330.

Rienecker, M. M. and Coauthors, 2008: The GOES-5 Data Assimilation System-Documentation of Versions 5.0.1, 5.1.0, and 5.2.0. NASA Tech. Rep. NASA/TM-2009-104606, Vol. 27, 118 pp.

Rose, F., D. A. Rutan, T. P. Charlock, G. L. Smith, and S. Kato, 2012: An algorithm for the constraining of radiative transfer calculations to CERES observed broadband top of atmosphere irradiance, submitted to *J. Atmos. Oceanic Technol.*

Rutan, D., F. Rose, M. Roman, N. Manalo-Smith, C. Schaaf, and T. Charlock, 2009: Development and assessment of broadband surface albedo from Clouds and the Earth's Radiant Energy System clouds and radiation swath data product. *J. Geophys. Res*., 114, D08125, doi:10.1029/2008JD010669.

Sohn, B. J., T. Nakajima, M. Satoh, and H.-S. Jang, 2010: Impact of different definitions of clear-sky flux on the determination of longwave cloud radiative forcing: NICAM simulation results. *Atmos. Chem. Phys*., 10, 11641-11646, doi:105194/acp-10-11641-2010.

Toon, O. B., C. P. Mckay, T. P. Ackerman and K. Santhanam, 1989: Rapid calculation of radiative heating rates and photodissociation rates in inhomogeneous multiple scattering atmospheres. *J. Geophys. Res.,* 94**,** 16 287–16 301.

Yang, S.-K., S. Zhou, and A. J. Miller, 2000: SMOBA: A 3-D daily ozone analysis using SBUV/2 and TOVS measurements. http://www.cpc.ncep.noaa.gov/products/stratosphere/SMOBA/smoba_doc.shtml.

6.0 Attribution

When referring to the CERES EBAF-Surface product, please include the data set version and the data product as “CERES EBAF-Surface_Ed2.6r.”

The CERES Team has made considerable efforts to remove major errors and to verify the quality and accuracy of this data. Please provide a reference to the following paper when you publish scientific results with the

CERES EBAF-Surface_Ed2.6r

Kato, S., N. G. Loeb, F. G. Rose, D. R. Doelling, D. A. Rutan, T. E. Caldwell, L. Yu, and R. A. Weller, 2012a: Surface irradiances consistent with CERES-derived top-of-atmosphere shortwave and longwave irradiances, *J. Climate*, in press.

When CERES data that are obtained via the CERES web site are used in a publication, we request the following acknowledgment be included: "These data were obtained from the NASA Langley Research Center CERES ordering tool at (http://ceres.larc.nasa.gov/)."

7.0 Feedback and Questions

For questions or comments on the CERES EBAF-Surface Data Quality Summary, please contact Dr. Seiji Kato, seiji.kato@nasa.gov. For questions about the CERES subsetting/visualization/ordering tool at http://ceres.larc.nasa.gov/order_data.php, please click on the "Feedback" link on the left-hand banner.